Blister resistant targets for nuclear reaction experiments with α-particle beams

Sean Hunt [a,c,*], Camden Hunt [b], Christian Iliadis [a,c], Michael Falvo [a]

[a] Department of Physics and Astronomy, The University of North Carolina at Chapel Hill, Chapel Hill, NC 27599, USA
[b] Department of Chemistry and Biochemistry, University of California, Santa Barbara, Santa Barbara, CA 93106, USA
[c] Triangle Universities Nuclear Laboratory, Durham, NC 27708, USA

ARTICLE INFO

Keywords:
Nuclear targets
Blistering
α particles
Fused silica
Sintered metal
Porous metal

ABSTRACT

Solid targets for nuclear measurements that use α-particle beams commonly experience a form of degradation known as blistering. The effect can prevent the use of solid targets for high intensity α-particle experiments, often necessitating complex gas target systems. To combat this problem, three different blister resistant target backings were designed for use in direct reaction measurements with high intensity α-particle beams. The blister resistant target designs utilize gas diffusive properties of fused silica, sintered metal, and porous evaporated metal. Each target was implanted with ^{22}Ne ions and bombarded with α-particle beam to test blister resistance. Targets were characterized and monitored using the ^{22}Ne$(p,\gamma)^{23}$Na reaction to determine the degradation of implanted material, and compare them to typical implanted noble gas targets. We find that all targets studied exhibit resistance to blistering, with the porous evaporated metal targets displaying the least amount of target material degradation.

1. Introduction

The majority of targets used in the measurement of charged-particle nuclear reactions are fabricated by depositing target material on solid backings [1], e.g., via implantation or evaporation. Metals, such as tantalum, nickel, titanium, and copper, are common choices for backings because they have high melting points, low contaminant content, high electrical conductivity, and high thermal conductivity [2,3].

It has long been known that intense α-particle bombardment of metal backings can cause significant target degradation through *blistering* [4–8]. Fig. 1 illustrates the effect and the resulting destruction of surface target material. High pressure helium bubbles from α-particle bombardment form within the metallic lattice, as depicted in part (a). Once enough pressure has built, the bubbles burst through the face of the target, destroying the surface of the target backing and resulting in a significant loss of implanted or evaporated target material, as illustrated in part (b).

Blistering is distinct from damage caused by excessive power deposition from intense particle bombardment on the target. Damage from excessive power deposition, referred to in this study as *heat damage*, can occur with an incident beam of any particle type. On the other hand, blistering only occurs when certain gases are implanted into metals, and usually results in burn marks on the target and a steady decrease of target material with continued ion bombardment.

This study focuses on attempts to reduce or eliminate target blistering by developing solid target backings that prevent the formation of helium bubbles within their atomic lattice. In Section 2, we will discuss blistering in more detail. Section 3 discusses the ion accelerators used in the presented measurements. Section 4 explores the design and testing of three types of blister-resistant targets: fused silica (Section 4.1); sintered metal (Section 4.2); and porous evaporated titanium (Section 4.3), which proved to be the most successful target developed in this study. Atomic force microscope images of the latter target are presented in Section 4.4. Section 5 provides a summary and conclusions.

2. Blistering

When helium is implanted into a metal, it migrates through the atomic lattice until it encounters a structural imperfection, called a loop dislocation. At a certain dose of implanted ions, the pressure inside the dislocation is sufficient to "punch" out of the loop dislocation (*loop punching*) to form a bubble. This limiting pressure is given by [9]

$$P = \frac{2\gamma + \mu b}{R} \tag{1}$$

where γ is the surface free energy, b is the Burgers vector (representing the magnitude and direction of a lattice distortion resulting from a dislocation), μ is the sheer modulus, and R is the bubble radius. Typical pressures for bubble formation using this model range from 9 GPa in aluminum to 40 GPa in molybdenum.

* Corresponding author at: Department of Physics and Astronomy, The University of North Carolina at Chapel Hill, Chapel Hill, NC 27599, USA.
E-mail address: sean.hunt@unc.edu (S. Hunt).

https://doi.org/10.1016/j.nima.2018.12.005
Received 2 November 2018; Accepted 3 December 2018
Available online 10 December 2018

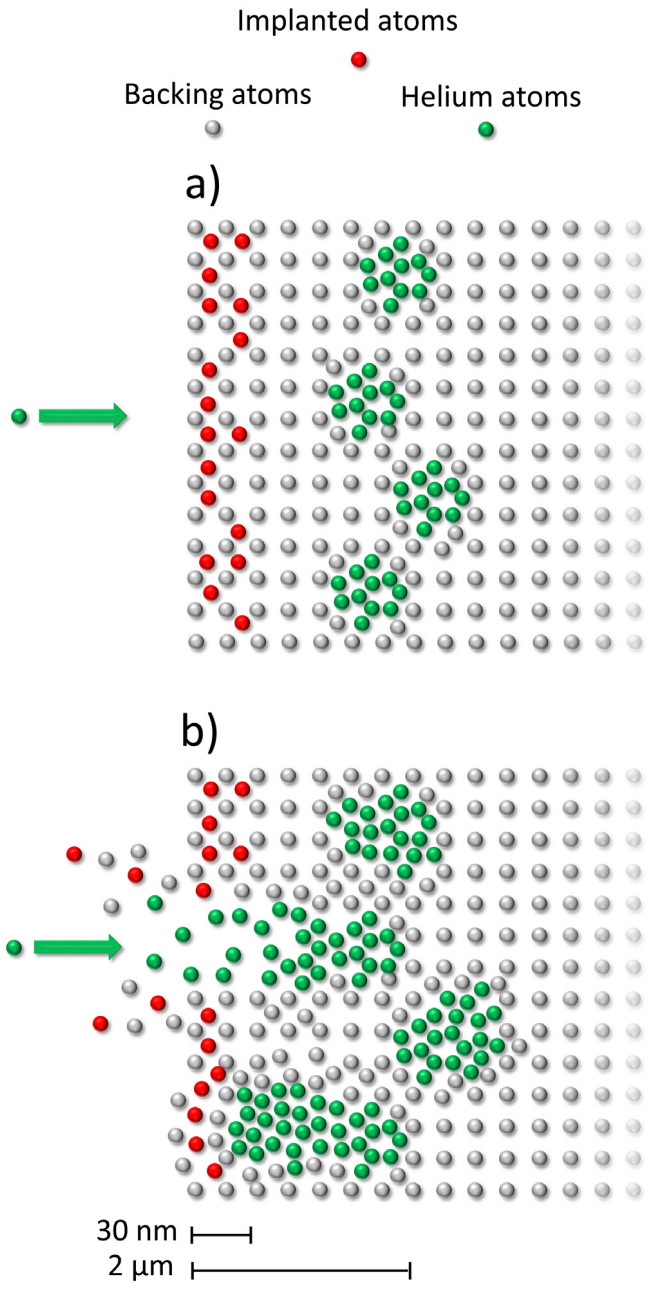

Fig. 1. Illustration of blistering in a metal target of crystal structure. (Gray) Metal backing atoms; (Red) Implanted target atoms; (Green) Helium atoms. (a) Bubble formation during α-particle bombardment, but before blistering occurs. (b) Destruction of the surface of the implanted target once the helium bubbles grow large enough to rupture through the surface . (For interpretation of the references to color in this figure legend, the reader is referred to the web version of this article.)

If helium is implanted continuously after the formation of a bubble, the bubble will continue to grow. It has been shown [10] that the modified van der Waals equation of state, given by

$$P' = \frac{nkT}{V - nB} \tag{2}$$

accurately approximates the behavior of helium inside the bubble. Here, P' is the pressure inside the bubble, T is the temperature, B is the van der Waals volume correction coefficient, k is the Boltzmann constant, and n is the particle number in moles.

At bombarding energies in the million electron volt range, small bubbles ($R < 2$ nm) form close to the metal backing surface (within ≈5 μm). Continuous α-particle bombardment will cause the bubbles to grow, according to Eq. (2) with internal pressures limited by Eq. (1). With enough bombardment, the bubbles rupture through the surface of the target, resulting in a significant loss of evaporated or implanted target material.

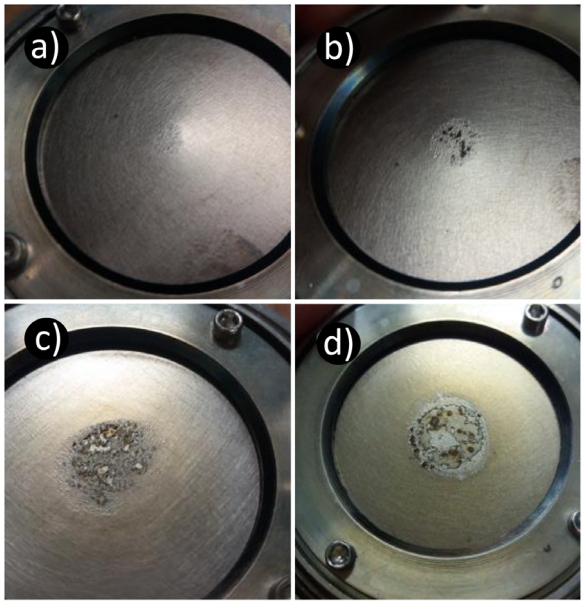

Fig. 2. Example of the progression of blistering in a titanium backing implanted with ^{22}Ne ions caused by the bombardment with α-particles of 900 keV energy. The α-particle intensity was kept low, near 30 μA, to prevent heat-related damage to the target. Panels (a), (b), (c), and (d) correspond to accumulated charges of 0.2 C, 0.4 C, 0.6 C, and 0.8 C, respectively. The effects of blistering in the center region become more apparent with increasing charge accumulation. After an accumulated charge of 0.8 C, the target is heavily damaged.

Fig. 2 depicts the progression of blistering in a titanium backing implanted with ^{22}Ne ions during bombardment with 900 keV α-particles. Panels (a), (b), (c), and (d) show the same target after an accumulated ion beam charge of 0.2 C, 0.4 C, 0.6 C, and 0.8 C, respectively. The images demonstrate the visible changes to the surface of the target, but it should be noted that significant degradation of implanted target material (^{22}Ne; see below) can be observed with as little as 0.1 C of accumulated charge.

3. Accelerators

The targets in this study were fabricated by implanting ^{22}Ne ions into backings using two different accelerators. An Eaton NV-3206 ion implanter with a modified end station, located at the University of North Carolina at Chapel Hill, was capable of accelerating 20 μA of singly-charged ^{22}Ne ions up to an energy of 200 keV. Targets were also implanted using the Electron Cyclotron Resonance Ion Source (ECRIS) at the Laboratory for Experimental Nuclear Astrophysics (LENA), located at the Triangle Universities Nuclear Laboratory [11]. The ECRIS is capable of accelerating 70 μA of ^{22}Ne ion with energies up to 200 keV. All targets in this study were implanted at an energy of 75 keV using the maximum beam intensity available at each accelerator.

Targets were tested and characterized using a 1 MV model JN Van de Graaff accelerator located at LENA. The machine is capable of accelerating singly-charged helium ions with a beam intensity of up to 120 μA on target. The helium beam was used to study the effects of blistering in different types of backings. The JN accelerator is also capable of producing proton beams with a maximum current of ≈150 μA on target, and a 1–2 keV spread in beam energy. The proton beam was used to characterize the targets (i.e, the concentration of ^{22}Ne ions), by measuring the 479 keV (laboratory frame) resonance in the ^{22}Ne$(p,\gamma)^{23}$Na reaction. The γ-ray monitored for the yield curve had an

energy of 6270 keV, corresponding to the 9252 → 2982 keV primary transition in ^{23}Na [12]. The γ-rays were measured using LENA's coaxial high purity germanium (HPGe) detector with a relative efficiency of 135% [13]. The detector was located in close geometry to the target at an angle of 0° relative to the incident ion beam direction.

The target was held at the end of a liquid-nitrogen cooled copper shroud, which reduces contaminant buildup on the target. Incident particle beams traveled through a 1.27-cm diameter collimator placed before the target. The collimator defined the beam spot on the target. A secondary electron suppression ring, located just before the target, was biased to −300 V and prevented emission of secondary electrons from the target and collimator. The vacuum pressure in the target chamber was maintained at $\approx 5 \times 10^{-7}$ Torr by a turbo pump and oil-less scroll pump. The target was cooled with de-ionized chilled water circulating in a closed loop to ensure all charge collected on the target passed through the current integration system.

4. Blister-resistant targets

To illustrate the loss of target atoms caused by blistering in a typical nuclear reaction experiment, we first prepared a target by implanting ^{22}Ne ions into a 0.5 mm thick tantalum backing with an incident dose of ≈0.45 C. The yield curve (i.e., the ^{22}Ne concentration profile), measured using the 479 keV (laboratory frame) resonance in ^{22}Ne$(p,\gamma)^{23}$Na, is shown in Fig. 3a. The ^{22}Ne has a thickness of ≈10 keV, and the observed maximum yield of the 6270 keV γ-ray from the decay of ^{23}Na corresponds to a stoichiometry of ≈ $^{22}Ne_1Ta_3$. After this measurement, we exposed the target to an α-particle beam of 900 keV energy and 30 μA intensity, resulting in a total accumulated charge of 0.5 C. We then attempted to measure another ^{22}Ne$(p,\gamma)^{23}$Na yield curve, but only upper limits for the intensity of the 6270 keV γ-ray could be obtained (blue data points in Fig. 3a). In other words, blistering during α-particle bombardment had removed all implanted ^{22}Ne atoms.

In the following subsections, we discuss our efforts to fabricate blister-resistant targets.

4.1. Fused silica targets

Fused silica, sometimes referred to as fused quartz, is a glass (amorphous silicon dioxide) that is formed by melting a silicon-rich chemical precursor in combination with flame oxidation at temperatures around 1700 K [14]. The lack of additives typically used in glass-making to lower the melting point (such as borontrioxide, metaphosphates, or sodium compounds) results in a clear glass that is low in contaminants and has a very high gas diffusion coefficient [15–17]. The high diffusion coefficient (the exact value for helium is dependent on temperature, with ranges of ≈0.25 600 $\times 10^{-7}$ cm^2/s for temperatures between 25–1000 C [15]) allows the implanted, electrically-neutralized α-particles to disperse throughout the backing and into the water cooling system on the back face of the target, preventing bubble formation and associated blistering. The situation is shown schematically in Fig. 4.

Fused silica has long been studied as a material to contain high level nuclear waste, in part because of the high helium diffusion coefficient reduces the damage from blistering [18]. In addition to high gas diffusion rates, fused silica can be made chemically pure, thereby reducing the ion-beam-induced background in a nuclear reaction measurement. For more details on the types of fused silica glass and their associated impurities, see Ref. [19].

The fused silica backings used in our experiment were discs with a diameter of 3.81 cm, and a thickness of 1.59 mm, made of ground and polished GE 124 glass[1] purchased from Technical Glass Products®. An image is shown on the right side in panel (a) of Fig. 5. A thin surface

[1] The manufacturer provided the following tracer element concentrations (in parts-per-million): OH^- (33); Al (20.3); Ca (1.8); Fe (1.9); Li (1.0); Mg (0.5); Na (1.3); Ti (1.4).

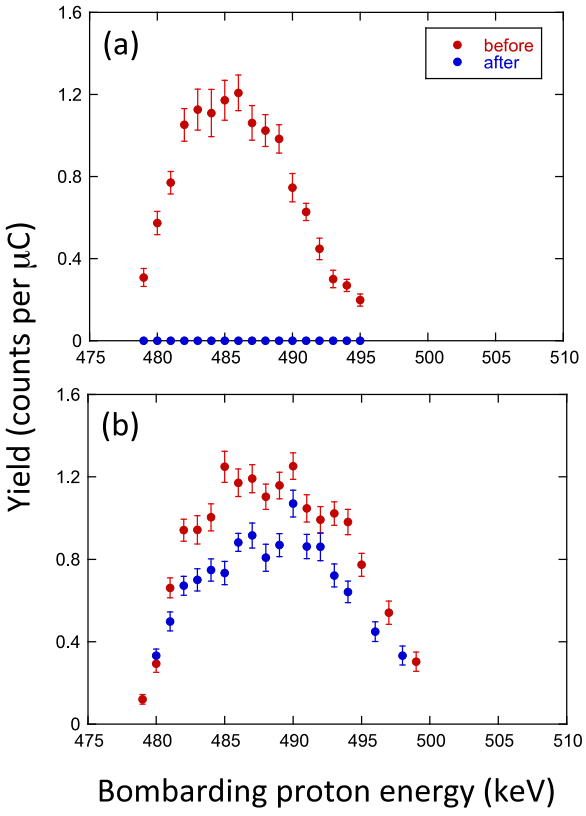

Fig. 3. Yield curves for the 479 keV (laboratory frame) resonance in ^{22}Ne$(p,\gamma)^{23}$Na, measured by using the observed intensity of the 6270 keV γ-ray from the decay of ^{23}Na. The red and blue data points correspond to the yield before and after α-particle bombardment. (a) Tantalum sheet implanted with ^{22}Ne ions. Notice that only upper limits for the yield could be obtained after α-particle bombardment with an accumulated charge of 0.5 C (blue data points), demonstrating the severe loss of ^{22}Ne concentration caused by blistering. (b) Fused silica target implanted with ^{22}Ne ions. The maximum yield declines by ≈20% after α-particle bombardment with an accumulated charge of 0.65 C . (For interpretation of the references to color in this figure legend, the reader is referred to the web version of this article.)

metal layer must be evaporated onto the fused silica backing to hold the implanted ^{22}Ne atoms, since noble gases implanted directly into the fused silica would diffuse through the matrix. This layer must be thin enough to allow the α-particles to pass through before coming to a stop within the fused silica backing, and also be thick enough to hold the desired layer of implanted target material (Fig. 1). Titanium was chosen for this study because it has a lower effective stopping power than most metals, resulting in a higher nuclear reaction yield [1].

The projected range of 900 keV α particles in titanium metal is ≈2 μm, according to the SRIM package [20]), while the projected range of ^{22}Ne ions implanted at 100 keV is ≈30 nm. Therefore, we evaporated a 200 nm thick layer of titanium onto the fused silica backing. This layer also allowed for integrating the current deposited by the ion beam, despite the fact that fused silica is an electrical insulator by providing the charge deposited by the incident α particles a short path to ground (≈3 μm, the penetration depth of the α particles in fused silica after losing energy in the titanium layer).

The smooth surface of the fused silica has a tendency to cause the evaporated titanium layer to peel away. For this reason, the fused silica backing was "frosted" using a 20 psi glass bead blaster before evaporation. This process creates a pitted glass surface that the titanium can better affix to. An image of a frosted backing is shown on the left side in panel (a) of Fig. 5. It should be noted that excessive frosting of the glass can weaken the backing. If high pressure (> 40 psi) water is used for target cooling, frosting should be kept to a minimum to prevent the

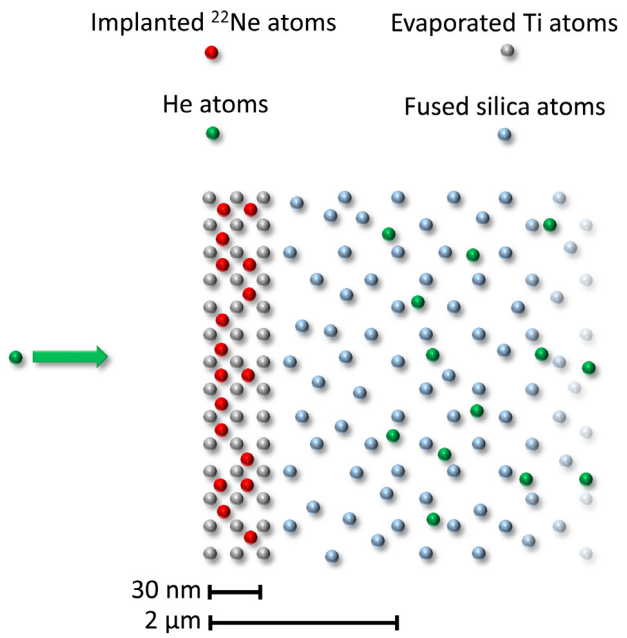

Fig. 4. Structure of a fused silica target. (Light blue) Fused silica backing atoms forming an amorphous matrix; (Gray) Evaporated Ti atoms; (Red) Implanted ^{22}Ne atoms; (Green) Helium atoms. The incident helium atoms diffuse quickly through the fused silica matrix, which prevents high-pressure bubbles from forming. Compare this situation with the one depicted in Fig. 1 . (For interpretation of the references to color in this figure legend, the reader is referred to the web version of this article.)

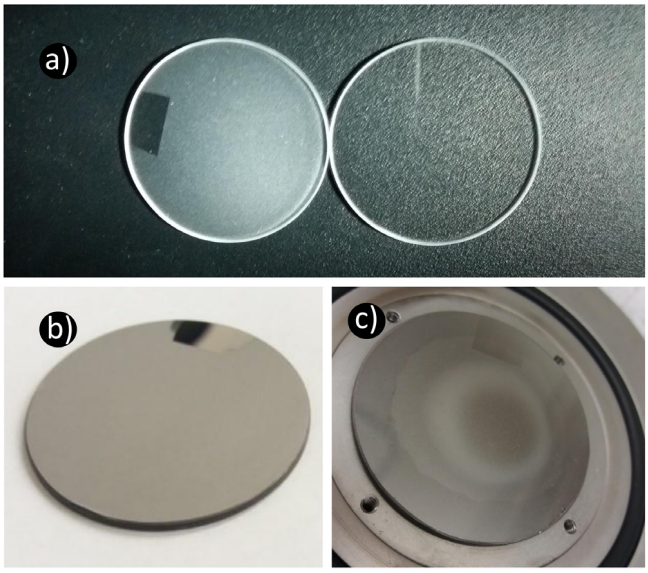

Fig. 5. Preparation of a fused silica target. (a) Fused silica backings before (right) and after (left) being frosted using a glass bead blaster. (b) Frosted fused silica backing after evaporation of a thin titanium layer. (c) Target after implantation of ^{22}Ne into the thin titanium surface layer.

backing from fracturing under the differential pressure of the vacuum on one face and water cooling on the opposite face.

After a thin titanium layer was evaporated onto the frosted glass surface, it was implanted with ^{22}Ne ions using a dose of ≈1 C (Section 3). Images of the evaporated and implanted surfaces are shown in panels (b) and (c) of Fig. 5.

Yield curves of the ^{22}Ne$(p,\gamma)^{23}$Na reaction are displayed in Fig. 3b. The red points show the yield before any α-particle bombardment. This target is thicker compared to the implanted tantalum target (Fig. 3a) because of the larger range of ^{22}Ne ions in titanium compared to tantalum. However, the heights of the yield curves (red points in Fig. 3) are comparable. For the fused silica target, the measured maximum yield corresponds to a stoichiometry of $\approx {}^{22}\mathrm{Ne}_1\mathrm{Ti}_5$.

The fused silica target was then exposed to a 900-keV energy α-particle beam with an intensity of 30 μA. The total accumulated charge was 0.65 C. No visible marks of blistering, such as those shown in Fig. 2, were observed on the target surface after α-particle bombardment. A second yield curve was measured after α-particle bombardment, which is displayed as the blue data points in Fig. 3b. It can be seen that the maximum yield degraded by ≈20% after α-particle bombardment. This result represents a significant improvement over the implanted tantalum target, which showed a complete loss of the implanted ^{22}Ne concentration after a similar accumulated α-particle charge.

Signs of heat damage (Section 1) in the form of minor burn marks on the surface and an odor of burnt metal were noticed when the target was removed from the vacuum chamber after α-particle bombardment. Fused silica have a relatively low coefficient of thermal conductivity ($\approx 2.7\times10^{-3}$ cal cm^{-1} s^{-1} K^{-1} [21]), which prevents these targets from withstanding high ion beam powers. Further tests indicated that heat damage starts to become noticeable at beam powers > 25 W cm^{-2}, corresponding to an α-particle beam of ≈30 μA intensity at 900 keV energy.

Fused silica targets exhibit significant blister resistance, and have low contaminant concentrations [19]. Therefore, they will likely be advantageous in many nuclear physics experiments that utilize moderate beam intensities. However, these targets will be subject to heat damage at high beam powers in excess of 25 W cm^{-2}.

4.2. *Sintered metal targets*

Sintered metal is produced by compacting and molding a mass of small metal grains, typically with pressure or heat, without reaching the melting point. The result is a porous matrix, and a target can be produced by implanting ions into the surface layer of such a backing. The situation is illustrated in Fig. 6, showing a titanium sintered backing (gray) with a ^{22}Ne-implanted surface region (red), which is exposed to a helium ion beam (green). The beam traverses the target region and comes to a stop deeper inside the sintered backing. High-pressure helium bubbles may form inside the grains. When the bubbles explode, they will burst into the inter-grain pore space, without damaging the implanted target surface. The size of the grains is important in this regard. If the grain size is smaller than the size of the bursting helium bubbles (<100 nm; see Section 2), loop punching may not occur as helium atoms diffuse through the sintered matrix rather than congregate at lattice impurities (Section 2).

Sintered metals are typically sold based on pore size (usually between 3 nm and 200 μm). We purchased sintered titanium metal discs with a diameter of 3.81 cm and a thickness of 1.59 mm from Porvair Filtration Group®. The average pore size was 100 nm.

Because of the porous nature of sintered metal, it is not possible to directly water cool the back of the target and maintain vacuum. Therefore, we sealed the back of the target by affixing a 0.5 mm thick nickel sheet with Armstrong A-12 Epoxy® to the sintered titanium backing. The nickel sheet was then exposed to direct water cooling during our measurements. Fig. 7 shows the round sintered titanium disk mounted atop a square nickel sheet.

The sintered titanium backing was implanted with singly-charged ^{22}Ne ions using a dose of ≈1 C (Section 3). Yield curves of the 479 keV resonance in ^{22}Ne$(p,\gamma)^{23}$Na are displayed in Fig. 8a. The red data points show the reaction yield before any α-particle bombardment. The target was then exposed to an α-particle beam of 400 keV energy and 50 μA intensity for a total accumulated charge of 0.5 C.[2]

[2] Problems with the accelerator prevented us from using an α-particle beam of 900 keV for this measurement. However, it has been shown that helium bubble formation in metals occurs at all bombarding energies [22]. Furthermore, we have observed blistering with a 400-keV α-particle beam incident on an implanted tantalum target.

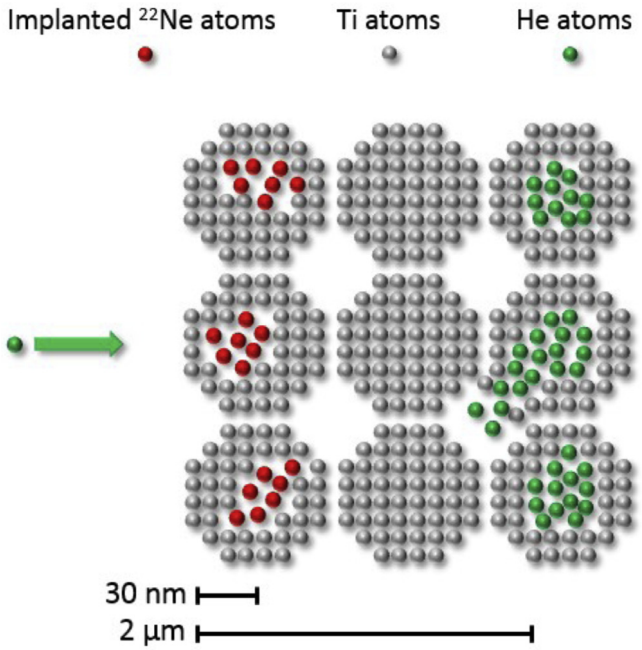

Fig. 6. Structure of a sintered titanium target. (Gray) Titanium atoms, forming grains of a crystal structure. The grains are separated by cavities (pores) (Red) Implanted ^{22}Ne atoms; (Green) Helium atoms. Helium bubbles form in the titanium grains, and burst into the inter-grain volume, preventing damage to the implanted target material near the surface . (For interpretation of the references to color in this figure legend, the reader is referred to the web version of this article.)

Fig. 7. Sintered titanium target. The round disk is the sintered titanium backing, and the irregular dark spot on the surface is the region with implanted ^{22}Ne atoms. The brown square around the disc is epoxy affixing it to the square nickel sheet. The target holder is seen behind the target . (For interpretation of the references to color in this figure legend, the reader is referred to the web version of this article.)

A second ^{22}Ne$(p,\gamma)^{23}$Na yield curve was then measured, which is shown as the blue data points in Fig. 8a. It can be seen that the maximum yield decreased by ≈20%. The magnitude of the degradation is similar to the result for the fused silica target (Section 4.1 and Fig. 3b), but nevertheless represents a significant improvement over the performance of an implanted tantalum sheet (Fig. 3a) that exhibited a complete loss of implanted ^{22}Ne atoms after a similar incident α-particle dose.

No visible effects of blistering, such as those shown in Fig. 2, were observed on the target surface after α-particle bombardment. However, as was the case for the fused silica target (Section 4.1), we observed

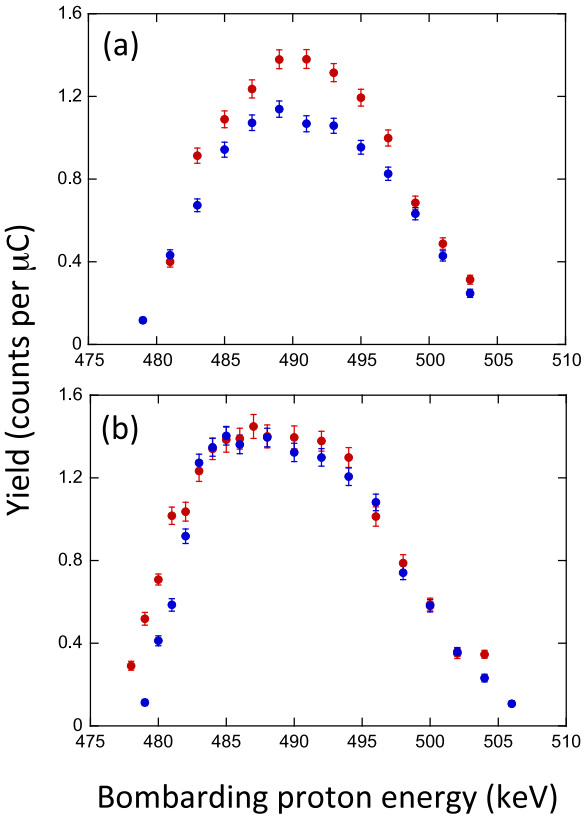

Fig. 8. Yield curves for the 479 keV (laboratory frame) resonance in ^{22}Ne$(p,\gamma)^{23}$Na, measured by using the observed intensity of the 6270 keV γ-ray from the decay of ^{23}Na. The red and blue data points correspond to the yield before and after α-particle bombardment. (a) Sintered titanium backing implanted with ^{22}Ne ions. The maximum yield declines by ≈20% after α-particle bombardment with an accumulated charge of 0.5 C. (b) Porous titanium target implanted with ^{22}Ne ions. Notice that the maximum yield height does not change after α-particle bombardment with an accumulated charge of 1.5 C . (For interpretation of the references to color in this figure legend, the reader is referred to the web version of this article.)

minor burn marks and an odor of burnt metal after the target was removed from the vacuum chamber. Further tests showed that an α-particle beam power exceeding 20 W cm^{-2} will result in heat damage to the sintered titanium target. This effect, rather than blistering, is the suspected cause of the decline in the maximum yield shown in Fig. 8a.

Sintered metals have been shown to have a lower thermal conductivity than solid metals. The thermal conductivity is inversely proportional to the porosity (up to a reduction factor of 3 at 45% porosity; see Fig. 3 of Ref. [23]). This is partly because of the lower density, and partly because of insulating gases present within the intergrain space [23,24]. Insulating gases are absent in the environment of the vacuum chamber. Although the thermal conductivity of sintered metals in a vacuum is not well measured, it is likely that the lower density will contribute to a lower overall thermal conductivity when compared to a solid metal backing. The observed heat damage could potentially be mitigated by either utilizing a sintered metal of higher thermal conductivity (e.g., nickel or tantalum), or by using thinner sintered metal discs.

In addition, the epoxy affixing the sintered titanium backing to the water-cooled titanium sheet (Fig. 7) will contribute to a decrease in the thermal conductivity of the target. A better method of sealing the back surface of the backing will likely improve the thermal conductivity.

4.3. *Porous metal targets*

When a metal layer is evaporated at a slow rate (several nanometers per minute) onto a heated metal surface, it can form a porous structure

Table 1
Summary of present results. All targets were implanted with ^{22}Ne ions of 75 keV energy and incident dose of between 0.5 and 1 C.

Target/backing	Stoichiometry[a] $^{22}Ne_x(matrix)_y$	Charge/energy[b] (C)/(keV)	Beam power[c] (W cm^{-2})	Target loss[d] (%)
Ta	$^{22}Ne_1Ta_{2.6\pm0.4}$	0.50/900	40	≈100
Fused silica	$^{22}Ne_1Ti_{4.9\pm0.7}$	0.65/900	25	18 ± 5
Sintered Ti	$^{22}Ne_1Ti_{3.6\pm0.5}$	0.50/400	20	22 ± 7
Porous Ti	$^{22}Ne_1Ti_{3.8\pm0.6}$	1.5/900	40	≈0

[a]Derived from maximum height of measured ^{22}Ne(p,γ) ^{23}Na yield curve (see Eq. (4.116) in Ref. [1]).

[b]Accumulated charge and energy of incident He^+ ions on target.

[c]Helium beam power deposited on target.

[d]Reduction in ^{22}Ne concentration as measured by the maximum yield before and after α-particle bombardment.

of interlocking metal crystals [25], also called porous metal. If the evaporated layer extends beyond the range of incident α particles, they come to rest within the interlocking crystal matrix. Helium bubbles will likely not form in such a medium during α-particle bombardment if the crystals are smaller than the typical diameter of helium bubbles in solid metals (Section 2). If, on the other hand, the crystals are larger than the helium bubbles, the latter will burst into the inter-crystal volume, thereby preventing blister damage to the implanted or evaporated material at the target surface.

We fabricated a porous titanium target as follows. A thick (>3 μm) layer of titanium was first evaporated onto a 0.5 mm thick titanium backing at a rate of ≈7 nm per minute. Subsequently, ^{22}Ne ions were implanted into the porous surface with an incident dose of ≈1 C. The morphology of the target surface will be discussed in Section 4.4.

Yield curves of the 479 keV resonance in $^{22}Ne(p,\gamma)^{23}Na$ are displayed in Fig. 8b. The red data points show the reaction yield before any α-particle bombardment. The target was then exposed to an α-particle beam of 900 keV energy and 50 μA intensity for a total accumulated charge of 1.5 C. A second $^{22}Ne(p,\gamma)^{23}Na$ yield curve was then measured, which is shown as the blue data points in Fig. 8b. It can be seen that the maximum yield did not change as a result of helium beam exposure.

We did not observe any visible signs of blistering on the target surface. Neither did we notice any signs of heat damage in the form of burn marks on the target surface or odor of burnt metal after removing the target from the vacuum chamber. The porous titanium target could withstand an α-particle beam power of 40 W cm^{-2}, corresponding to a bombarding energy of 900 keV and an intensity of ≈50 μA. Further tests showed that higher α-particle beam intensities resulted in signs of heat damage in the form of burn marks on the target surface. It appears likely that the heat damage could be reduced by increasing the thermal conductivity, either by using an improved target cooling design, or by preparing porous backings of metals with a higher thermal conductivity.

It should be noted that resistive evaporation is not the only method of fabricating a porous crystalline metallic structure, although it is convenient for metals with relatively low melting points. Electron beam evaporation or chemically induced crystal growth methods, such as de-alloying of NiM thin films [26,27] allow for greater control over deposition rate and crystal growth, and would produce targets with a higher thermal conductivity.

4.4. Atomic force microscopy

The porous titanium target showed the highest blister resistance, and, in addition, the lowest heat damage, of all targets investigated in this work. Therefore, we imaged the porous target to confirm the presence of surface structures, which would also imply the presence of subsurface porosity.

Surface morphology of evaporated metal films is highly dependent on evaporation rate, with slower deposition rates typically resulting in films with a smaller grain size and decreased surface roughness [28]. This can be attributed to a number of factors, including the evaporation rate-dependence of trace gas inclusion within the film (particularly oxygen) during vacuum vapor deposition, and the adatom (an atom on the surface of a crystal) diffusion rate relative to the evaporation rate [28,29]. Assuming Stranski–Krastanov (also known as "layer-plus-island") type growth [30], it is reasonable to assume that the subsurface porosity is correlated with the surface grain size.

To confirm the presence of Stranski–Krastanov structures, topographical data were collected with atomic force microscopy (AFM, MFP-3D Asylum Research, Santa Barbara, CA) in ambient laboratory conditions using oscillatory mode (AC, or tapping mode) imaging with silicon Olympus AC160 cantilevers, using a nominal resonance frequency ≈300 kHz, spring constant of ≈26 N m^{-1}, and tip radius of ≈10 nm. In typical imaging, the free oscillation amplitude was ≈100 nm and imaging was performed between 70 nm and 80 nm (70%–80% of the free oscillation amplitude). Images were taken at a fast scan axis frequency of 1 Hz. Just prior to collection of the data presented here, a calibration standard was imaged to verify accuracy of the data along the x, y, and z axes. The topographical data are accurate to <2%.

The AFM employed in this study used an optical lever method for monitoring calibrated cantilever motion (resolution < 1 nm) on a quadrant photo diode (QPD) sensor. The cantilever is driven just below resonance (at 95% of peak amplitude) and the sharp tip at the end of the cantilever is brought into intermittent contact with the surface, while the QPD monitors cantilever motion. A proportional–integral–derivative feedback loop controls a piezo translation stage that maintains an operator selected damping of the amplitude of the cantilever motion. As the sample is scanned beneath the tip, the feedback loop maintains a set point cantilever amplitude by modulating the height of the cantilever mount position with a calibrated (< 0.1 nm) piezo translation stage. The feedback driven movement of this piezo is what is collected as the topographical height data, and is combined with the (x, y) position of the sample to build a map of the sample surface topography.

Fig. 9 shows the images obtained by the atomic force microscopy measurements on four different samples. Panel (a) shows a blank titanium backing, revealing surface features typical of machine-cut stock sheet metal. Panel (b) depicts a layer of evaporated titanium. It appears to be composed of multiple interlocking titanium crystals, with an average size of ≈300 nm. Therefore, the image confirms the presence of a porous titanium layer. Panel (c) represents a porous titanium layer that was implanted with ^{22}Ne ions. Panel (d) shows an image after the target was bombardment with 0.5 C of α particles. It can be seen that the ^{22}Ne implantation appears to have sputtered away the surface layer, and the α-particle bombardment further modified the surface of the implanted region.

5. Conclusions

We discussed three different types of targets that show a significantly enhanced performance during α-particle exposure compared to conventional targets. We determined the effects of α-particle blistering for each target by measuring the concentration of implanted ^{22}Ne ions using the yield curve of the 479 keV resonance in the $^{22}Ne(p,\gamma)$ ^{23}Na reaction. A summary of our results is presented in Table 1. We conclude the following:

(i) Targets prepared by implanting ^{22}Ne into metals, such as Ta, show severe signs of blistering when exposed to intense α-particle beams. No noticeable ^{22}Ne concentration remains in the target after an α-beam accumulation of 0.5 C.

(ii) Fused silica targets do not appear to blister and can be fabricated chemically pure and low in contaminants, making them useful for α-particle experiments that are sensitive to beam-induced background. However, they show signs of heat damage at elevated deposited beam powers, and are also mechanically fragile.

(iii) Sintered Ti metal targets do not appear to blister under α-particle bombardment. They are physically more robust than fused silica targets.

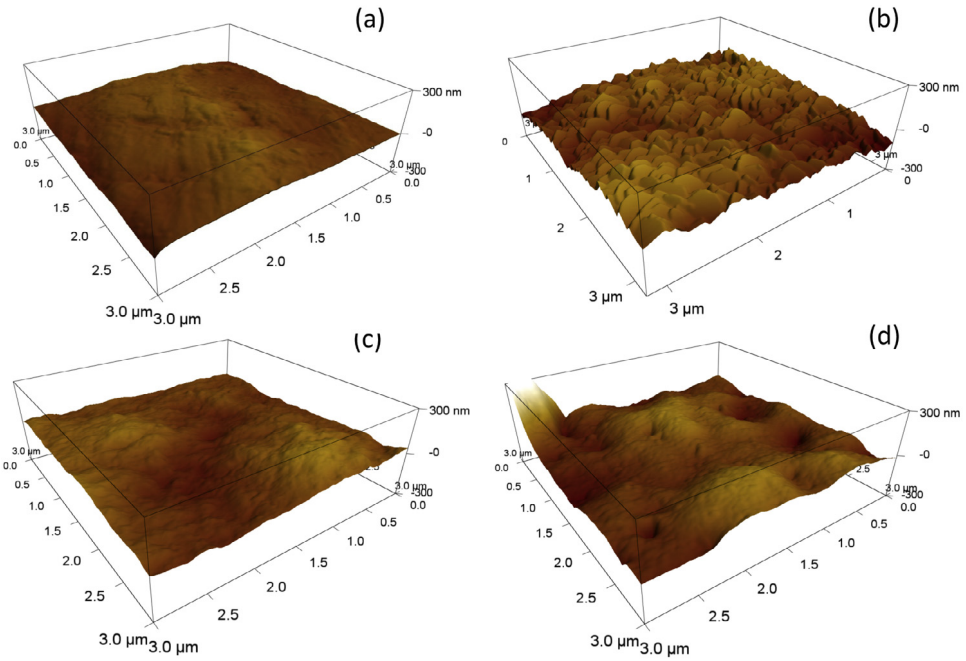

Fig. 9. Atomic Force Microscopy (AFM) images. (a) Blank titanium backing; (b) Evaporated titanium layer. Note the interlocking crystalline structure, indicating a porous material; (c) Evaporated titanium layer after implantation with ^{22}Ne ions. The surface layer has been sputtered away; (d) Evaporated layer that has been implanted with ^{22}Ne and then exposed to a 30 µA α-particle beam of 900 keV energy for a total accumulated charge of 0.5 C.

However, they did also show signs of heat damage at elevated deposited beam powers, which is likely caused by our method (using epoxy) of sealing the backface to allow for water cooling.

(iv) Evaporated porous Ti targets showed the greatest resistance to both blistering and heat damage. We suggest further investigation of this promising material, specifically to study the target stability for different pore sizes and the presence of contaminants that could give rise to beam-induced background.

Acknowledgments

We would like to thank A.E. Champagne, T.B. Clegg, R. Longland, L.N. Downen, A.L. Cooper, J.R. Dermigny, D.R. Little, and J.W. Mesrobian for their technical assistance, helpful comments, and discussions. This work was supported by the U.S. Department of Energy under contract No. DE-FG02-97ER41041.

References

[1] C. Iliadis, Nuclear Physics of Stars, second ed, John Wiley & Sons, 2015.
[2] J.S. Dugdale, The Electrical Properties of Metals and Alloys, Courier Dover Publications, 2016.
[3] F. Cverna, Thermal Properties of Metals, ASM International, Materials Park, OH, 2002.
[4] P. Johnson, R. Thomson, K. Reader, Tem and sem studies of radiation blistering in helium-implanted copper, J. Nucl. Mater. 273 (2) (1999) 117–129.
[5] M. Kaminsky, S. Das, Effect of temperature on first-wall erosion by radiation blistering, Nucl. Technol. 22 (3) (1974) 373–378.
[6] J. Evans, An interbubble fracture mechanism of blister formation on helium-irradiated metals, J. Nucl. Mater. 68 (2) (1977) 129–140.
[7] J. Evans, The role of implanted gas and lateral stress in blister formation mechanisms, J. Nucl. Mater. 76 (1978) 228–234.
[8] S. Erents, G. McCracken, Blistering of molybdenum under helium ion bombardment, Radiat. Eff. 18 (3–4) (1973) 191–198.
[9] H. Trinkaus, Energetics and formation kinetics of helium bubbles in metals, Radiat. Eff. 78 (1–4) (1983) 189–211.
[10] L. Mansur, W. Coghlan, Mechanisms of helium interactions with radiation effects in metals and alloys: A review, J. Nucl. Mater. 119 (1) (1983) 1–25.
[11] J. Cesaratto, A. Champagne, T. Clegg, M. Buckner, R. Runkle, A. Stefan, Nuclear astrophysics studies at lena: The accelerators, Nucl. Instrum. Methods Phys. Res. A 623 (3) (2010) 888–894.
[12] R. Longland, C. Iliadis, J. Cesaratto, A. Champagne, S. Daigle, J.R. Newton, R. Fitzgerald, Resonance strength in ne 22 (p, γ) na 23 from depth profiling in aluminum, Phys. Rev. C 81 (5) (2010) 055804.
[13] S. Carson, C. Iliadis, J. Cesaratto, A. Champagne, L. Downen, M. Ivanovic, J. Kelley, R. Longland, J.R. Newton, G. Rusev, et al., Ratio of germanium detector peak efficiencies at photon energies of 4.4 and 11.7 mev: Experiment versus simulation, Nucl. Instrum. Methods Phys. Res. A 618 (1) (2010) 190–198.
[14] F. Voorhees, J. Flamenbaum, P. Schultz, Method for producing high quality fused silica, uS Patent 3, 806, 570, 1974.
[15] D. Swets, R. Lee, R. Frank, Diffusion coefficients of helium in fused quartz, J. Chem. Phys. 34 (1) (1961) 17–22.
[16] R. Lee, R. Frank, D. Swets, Diffusion of hydrogen and deuterium in fused quartz, J. Chem. Phys. 36 (4) (1962) 1062–1071.
[17] J.S. Masaryk, R.M. Fulrath, Diffusivity of helium in fused silica, J. Chem. Phys. 59 (3) (1973) 1198–1202.
[18] H. Matzke, E. Vernaz, Thermal and physicochemical properties important for the long term behavior of nuclear waste glasses, J. Nucl. Mater. 201 (1993) 295–309.
[19] M.L. Ferreira Nascimento, E.D. Zanotto, Diffusion processes in vitreous silica revisited, Phys. Chem. Glasses-Eur. J. Glass Sci. Technol. B 48 (4) (2007) 201–217.
[20] J. Ziegler, J. Biersack, M. Ziegler, The stopping and range of ions in matter, srim, 2013, Website: http://www.srim.org.
[21] K.L. Wray, T.J. Connolly, Thermal conductivity of clear fused silica at high temperatures, J. Appl. Phys. 30 (11) (1959) 1702–1705.
[22] N. Marochov, P. Goodhew, A comparison of the growth of helium and neon bubbles in nickel, J. Nucl. Mater. 158 (1988) 81–86.
[23] V. Kononenko, V. Baranovskii, V. Dushchenko, Thermal conductivity of porous sintered iron, Powder Metall. Met. Ceram. 7 (3) (1968) 175–177.
[24] J. Januszewski, M. Khokhar, A. Mujumdar, Thermal conductivity of some porous metals, Lett. Heat Mass Transfer 4 (6) (1977) 417–423.
[25] E. Bauer, Phänomenologische theorie der kristallabscheidung an oberflächen. ii, Z. Kristallogr.-Cryst. Mater. 110 (1–6) (1958) 395–431.
[26] L. Wang, T.J. Balk, Synthesis of nanoporous nickel thin films from various precursors, Phil. Mag. Lett. 94 (9) (2014) 573–581.
[27] L. Sun, C.-L. Chien, P.C. Searson, Fabrication of nanoporous nickel by electrochemical dealloying, Chem. Mater. 16 (16) (2004) 3125–3129.
[28] K. Cai, M. Müller, J. Bossert, A. Rechtenbach, K.D. Jandt, Surface structure and composition of flat titanium thin films as a function of film thickness and evaporation rate, Appl. Surf. Sci. 250 (1–4) (2005) 252–267.
[29] K. Hofmann, B. Spangenberg, M. Luysberg, H. Kurz, Properties of evaporated titanium thin films and their possible application in single electron devices, Thin Solid Films 436 (2) (2003) 168–174.
[30] I.N. Stranski, L. Krastanow, Zur theorie der orientierten ausscheidung von ionenkristallen aufeinander, Mon.hefte Chem. Verwandte Teile Wiss. 71 (1) (1937) 351–364.